PAPER

Design and measurement of a tiny wideband antenna for deeply embedded biomedical devices

Engineering Research Express

PAPER

Design and measurement of a tiny wideband antenna for deeply embedded biomedical devices

RECEIVED
7 December 2024

REVISED
22 March 2025

ACCEPTED FOR PUBLICATION
23 April 2025

PUBLISHED
6 May 2025

Abdelmouttalib Bousrout[1], Asma Khabba[2,3], Atta Ullah[4], Saida Ibnyaich[3], Tomader Mazri[1], Mohamed Habibi[5] and Ahmed Jamal Abdullah Al-Gburi[6]

[1] Advanced Systems Engineering Laboratory, National School of Applied Sciences, Ibn Tofail University, Kenitra, Morocco
[2] Laboratory LAMIGEP, EMSI Marrakech, Marrakech, Morocco
[3] Instrumentation, Signals and Physical Systems (I2SP) Team, Faculty of Sciences SEMLALIA, Cadi Ayyad University, Marrakesh, Morocco
[4] Faculty of Engineering and Digital Technologies, University of Bradford, United Kingdom
[5] Laboratory of Electronic Systems, Information Processing, Mechanics and Energetics, Faculty of Science, Ibn Tofail University, Kenitra, Morocco
[6] Center for Telecommunication Research & Innovation (CeTRI), Fakulti Teknologi dan Kejuruteraan Elektronik dan Komputer (FTKEK), Universiti Teknikal Malaysia Melaka (UTeM), Durian Tunggal, Melaka 76100, Malaysia

E-mail: ahmedjamal@ieee.org **and** engahmed_jamall@yahoo.com

Keywords: biotelemetry, pacemakers, specific absorption rate, miniaturized antenna, wideband

Supplementary material for this article is available online

Abstract

The increasing demand for compact and efficient implantable medical devices has driven the development of advanced antenna solutions for biomedical applications. This study presents a novel wideband implantable antenna specifically tailored for scalp implantation, operating across two critical frequency ranges: the Industrial, Scientific, and Medical (ISM) band (2.4–2.48 GHz) and the midfield frequency range (1.45–1.6 GHz). The antenna's compact design, with overall dimensions of $3 \times 4 \times 0.5\ mm^3$, features a 0.25 mm thick dielectric layer constructed from Rogers 4350B ($\varepsilon_r = 3.66$, $\tan_\delta = 0.0031$) for both the substrate and superstrate. Innovative design elements, including open-ended slots in the radiating patch and closed-ended slots in the ground plane, contribute to its compact size, enhanced impedance matching, and improved bandwidth performance. The antenna achieves a peak gain of −19.92 dBi at 2.45 GHz and delivers an ultra-wide bandwidth of 1836.8 MHz, spanning from 1.0602 GHz to 2.8970 GHz. These characteristics ensure reliable operation in diverse implantation scenarios within the human body, while adhering to IEEE C95.1-2005 safety standards for specific absorption rate (SAR) compliance. Comprehensive performance evaluations were conducted using finite-element simulations in homogeneous tissue environments, employing HFSS and CST software. The simulated results aligned closely with experimental measurements, validating the design's accuracy and manufacturability. Additionally, a link budget analysis confirmed the antenna's ability to maintain a robust and reliable wireless telemetric connection, demonstrating its suitability for medical applications and ensuring safe, efficient communication.

1. Introduction

A number of reasons, including the ease that implantable medical devices (IMDs) offer to patients, researchers have been very interested in this field. These IMDs are used in many different medical fields, including but not limited to glucose monitoring [1], retinal prosthesis [2], and capsule endoscopy [3]. Advanced medical telemetry systems have emerged to address the challenges faced by patients with internal organ-related illnesses, who often need extended hospital stays for continuous monitoring. To enhance patient comfort and improve monitoring efficiency, recent research has focused on developing wireless patient monitoring systems. These innovative systems enable data collection from patients within the comfort of their homes, eliminating the need for prolonged hospitalization. The core of such systems involves implantable or ingestible medical sensing devices

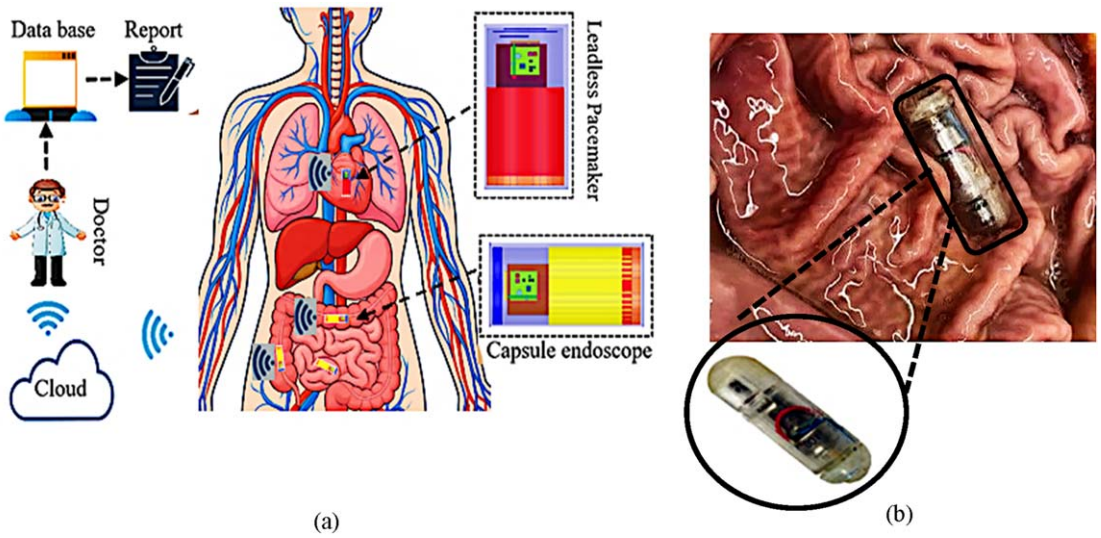

Figure 1. (a) Illustrating the wireless patient monitoring system with ingestible capsule and leadless pacemaker, and (b) concept real capsule position among gastric rugae in a swine stomach. From [12]. Reprinted with permission from AAAS.

placed inside the patient's body. These devices are outfitted with transmitters that facilitate wireless transmission of gathered data to external devices. Consequently, the data received can be smoothly relayed to medical institutions for immediate analysis and timely emergency notifications, thus optimizing the process of patient monitoring. The concept is visually represented in figure 1. Biomedical antennas face numerous challenges and constraints due to their operation within the highly complex and dissipative environment of the human body. Key considerations for implantable antennas include size, biocompatibility, impedance matching, link budget, and patient safety, making them a primary focus of research [4]. Implantable Medical Devices (IMDs) operate across various frequency ranges, with the Medical Implant Communication Service (MICS) band (402–405 MHz) being one of the most commonly used. This unlicensed spectrum is specifically allocated for medical applications. It is also important to note that each country has its own designated Industrial, Scientific, and Medical (ISM) bands. In the United States, the Federal Communications Commission (FCC) regulates the ISM bands, which span frequencies from 902–928 MHz and 2400–2483.5 MHz as reported in [5–7], the 2400–2483.5 MHz ISM band is often used by IMDs to switch between standby and active modes, which helps conserve battery power and prolong the lifespan of the device. Another frequently utilized band for wireless medical devices is the MedRadio band, which operates in the 401–406 MHz range. Comprehensive studies by respected researchers [8–10] have highlighted the inherent limitations of antennas operating within these frequency ranges, particularly concerning bandwidth. Consequently, these constraints may lead to reduced data transmission rates and limited image quality. The comprehensive design specifications for implanted antennas can be found in [11].

Patch antennas are commonly preferred for implantable applications due to their design flexibility and structural advantages [13]. Recent studies on medical implantable antennas, especially those addressing radio wave propagation through the human body, are discussed in [4]. Various implantable antenna designs for telemetry applications have emerged. For intracranial pressure (ICP) monitoring, a compact antenna with two communication channels (915 MHz and 2.45 GHz) demonstrated excellent gain and bandwidth [14]. Another study introduced a MIMO antenna for implants, operating at 2.45 GHz with a peak gain of −15.18 dBi, though its complexity and four-port power configuration reduced compatibility with modern IMDs [15]. A design for gastrointestinal endoscopy, operating within the ISM band (2.40–2.48 GHz), achieved a gain of −12 dBi and a bandwidth of 483 MHz, but was too large for smaller implants like wireless pacemakers [16]. Additionally, a dual-band antenna (7.2×0.2 mm^3) for implanted batteries showed significant gains at 928 MHz (25.65 dBi) and 2.45 GHz (28.44 dBi), although its SAR exceeded safe limits [17–21]. Another study proposed a small, circularly polarized antenna ($10 \times 10 \times 0.3$ mm^3) for biotelemetry, demonstrating a consistent gain of 7.79 dBi across its frequency range and including a SAR analysis [22]. However, as integrated wireless medical devices (IWMDs) often require multiple frequencies, single-band antennas are inadequate [23]. Dual- and triple-band antennas, though less common, are an area of growing interest. As stated in [24], the proposed implantable antenna is compact (17.15 mm^3) and operates across MICS, ISM, and midfield bands, showing satisfactory performance with peak gains of −30.5 dBi at 402 MHz and −18.2 dBi at 2450 MHz. However, the lower gain at higher frequencies may limit its communication range in certain applications. Another featured a dual-band antenna

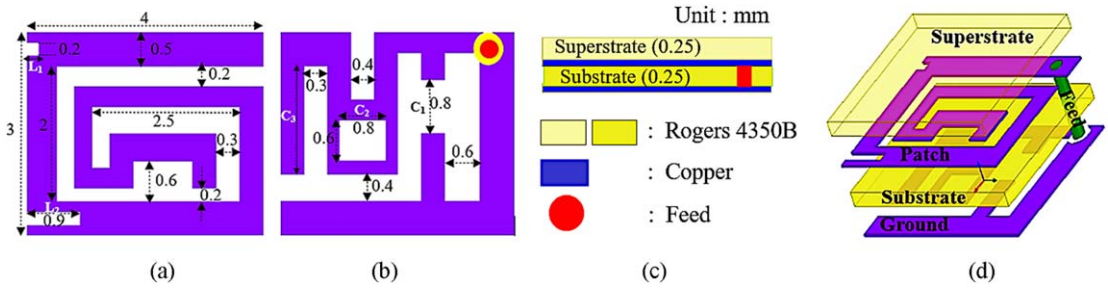

Figure 2. Geometry of the suggested antenna. (a) Front, (b) rear, (c) exploded, and (d) side views.

with a radiating slot patch aimed at improving power transfer efficiency with an external metallic reflector beneath the user's arm [25]. Finally, a self-duplexing implantable antenna with two ports was designed to minimize the physical footprint while maintaining performance, serving the dual functions of data transmission and RF energy harvesting [26]. However, the impedance bandwidths of these antennas remain somewhat limited, mainly due to the complex interactions with human tissues.

In the context of implantable medical devices (IMDs), antennas with expansive bandwidths are crucial for ensuring compatibility with designated frequency ranges and minimizing the impact of tissue-related challenges. This work centers on the design and evaluation of advanced biomedical antennas intended for deep implantation. A detailed review of current research highlights several key factors influencing antenna performance, including gain, radiation efficiency, impedance matching, sensitivity, and size. Taking these factors into account, an antenna was specifically designed to meet these demands, ensuring peak performance. The design emphasizes key attributes such as wide operational range, high gain, low Specific Absorption Rate (SAR), simplicity, and compact form. Through extensive simulations and real-world testing, the proposed antenna achieved a gain of −19.78 dBi at 2.4 GHz, providing a broad coverage bandwidth of 1836.8 MHz. Notably, this antenna features an ultra-compact design, with dimensions of just $3 \times 4 \times 0.5$ mm^3. These results mark a significant contribution to the field of biomedical antenna design, particularly for deeply embedded devices. The antenna's performance has been optimized to meet the unique requirements of such applications. The structure of this paper is as follows: The introduction outlines the growing importance of biomedical implants, with a focus on the radio communication aspect of these devices, their antenna requirements, and the challenges involved. It also reviews existing research, detailing their achievements and limitations, which served as a basis for this work. The second section describes the design methodology of the proposed antenna, including the simulation environment, experimental setup, and results from parametric analyses. This section also examines the coupling effects when the antenna is integrated into various implant types, such as pacemakers and endoscopic capsules. The following section explores the Specific Absorption Rate (SAR) of the antenna using a phantom model in a heterogeneous environment. The concluding section discusses the antenna's link budget, provides a comparative analysis, and includes final conclusions and references.

2. Methodology

2.1. Development and structure of the proposed wideband antenna and associated system

The selection of appropriate manufacturing materials is crucial for the design of implantable antennas. Flexible materials are recommended due to their ease of integration into biomedical devices and their compatibility with the human body [27, 28]. These materials exhibit resistance to dimensional and physical changes, enabling them to withstand muscle and tissue movements without compromising the antenna's performance [29]. The proposed ultra-miniaturized wideband (UWB) antenna, with its compact dimensions of $3 \times 4 \times 0.5$ mm^3, possesses intricate structural properties, as illustrated in figure 2. This design features a streamlined, meander-shaped patch that offers a low-profile form conducive to seamless circuit integration, making it ideal for applications such as wireless pacemakers and capsule endoscopes.

The strategically designed slots in the ground plane are essential for optimizing antenna performance and expanding its operational bandwidth, as illustrated in figures 2(a)–(d). The antenna is energized via a 50 Ω coaxial feed, with a diameter of 0.46 mm, located near the lower left corner of the patch antenna.

In practical applications, implanted antennas are not stand-alone entities; rather, they constitute integral elements within more extensive systems. In the course of our research, we have meticulously tailored the design of the suggested antenna to facilitate its harmonious integration with leadless cardiac pacemakers and wireless

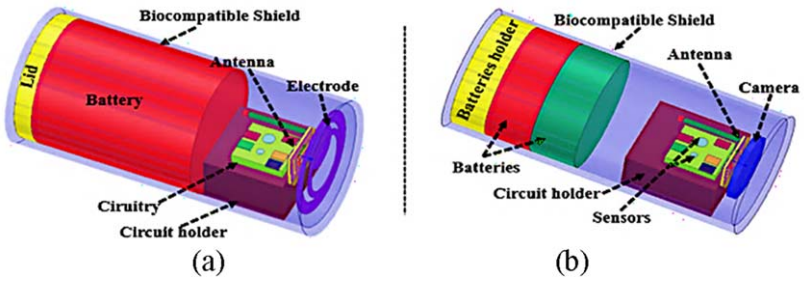

Figure 3. (a) Detailed architecture of the leadless pacemaker, and (b) the capsule endoscope.

capsule endoscopes. The visual representation of the proposed antenna's seamless integration with leadless pacemakers and capsule endoscopes is depicted in figure 3.

Within the capsule endoscopy equipment, three batteries constructed from perfect electric conductor (PEC) materials are strategically positioned. Additionally, a purpose-built transceiver has been incorporated into the system to enable the transmission and reception of electromagnetic signals. Furthermore, this capsule endoscope is equipped with cameras, LEDs, and image sensors. As stated in citation [30, 31], the device's housing is made from biocompatible alumina (Al2O3), with a thickness of 0.25 mm and a permittivity (ε_r) of 9.8. The leadless cardiac pacemaker (LCP) consists of components such as electrodes, circuit holder, antenna, container, circuitry, battery, and lid. Our models assume the electrodes, battery, and circuitry are made from high-conductivity materials, while the circuit holder uses Rogers RT/duroid 6010. Although other implant models may be similar, our goal is to understand the interactions between the antenna and these devices to assess their impact on antenna performance and ensure its proper function in realistic conditions.

2.2. Choice of frequency

Energy consumption is a significant challenge in the development of deeply implanted biomedical devices. To address this issue, a dual-band antenna design provides a pertinent solution by enabling the switch between sleep and active modes, thereby optimizing battery usage [32, 33]. This strategy extends the lifespan of the implanted devices and minimizes interference issues.In sleep mode, the antenna operates in the 2.4 GHz band without transmitting data, significantly reducing power consumption. When switched to active mode, the antenna transmits data at a frequency of 1.4 GHz. Therefore, this dual-band design ensures efficient energy management while maintaining reliable performance and optimal communication for deeply implanted biomedical devices.

2.3. Design process of the proposed antenna

The design of the proposed wideband antenna followed a systematic four-step optimization process, as illustrated in figure 4. The optimization of the proposed wideband antenna is based on the application of the Defected Ground Structure (DGS) technique, which involves introducing geometric defects in the ground plane to enhance the antenna's electromagnetic performance. By strategically modifying the ground plane, DGS enables resonance frequency tuning, optimizes impedance matching, and broadens the bandwidth. Unlike conventional methods that rely on capacitive elements, this approach achieves effective resonance shifts without introducing additional passive components such as capacitors or inductors [14, 27]. The implementation of DGS in this design consists of incorporating slots on both the radiating patch and the ground plane. These slots disrupt the surface current distribution, altering the effective electrical length of the patch and consequently shifting the resonance frequency. This modification not only improves impedance matching but also extends the current path, contributing to the enhancement of the antenna's overall performance. The reflection coefficient (S11) results at each optimization stage are presented in figure 5(a). The initial design featured a baseline configuration with slots on both the radiator and the ground plane. The choice of the spiral shape is based on its simple design and ease of fabrication. Additionally, a key advantage of this option lies in its intrinsic dispersion characteristics, which make spiral and meander antennas less affected by variations in the dielectric properties of the surrounding biological tissues [29]. In the first stage, a weak resonance was observed at 1.48 GHz with an S11 of −15 dB. In the second stage, the addition of extra slots introduced a secondary resonance at approximately 2.8 GHz, with an S11 of −9.98 dB. In the third stage, the integration of open-ended slots and a rectangular cut on the ground plane shifted the second resonance to 2.38 GHz and adjusted the lower resonance to 1.4 GHz, in accordance with theoretical predictions. This modification increased the structure's capacitance, thereby lowering the resonance frequency. Finally, in the fourth stage, fine-tuning adjustments resulted in an upper resonance around 2.45 GHz with an S11 of −26 dB and a lower resonance at 1.41 GHz with an S11 of −50 dB, achieving an extensive bandwidth of 1836.8 MHz.

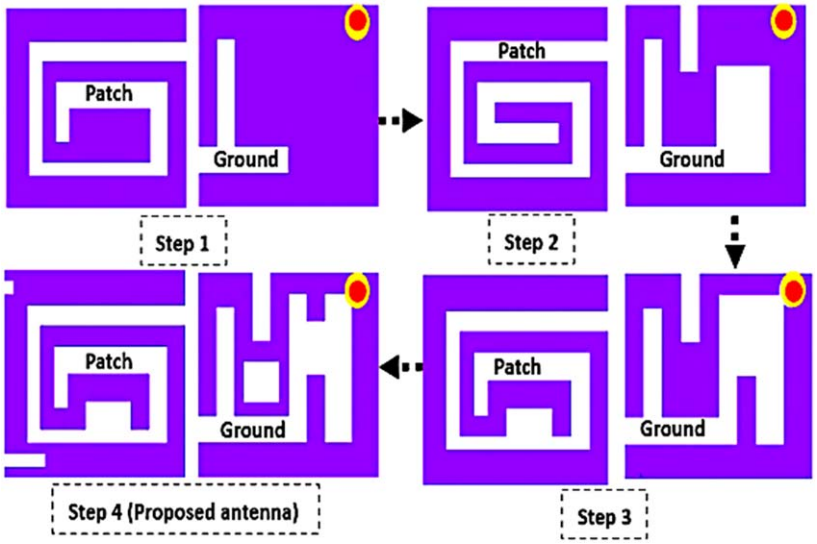

Figure 4. Designing steps of the wideband antenna.

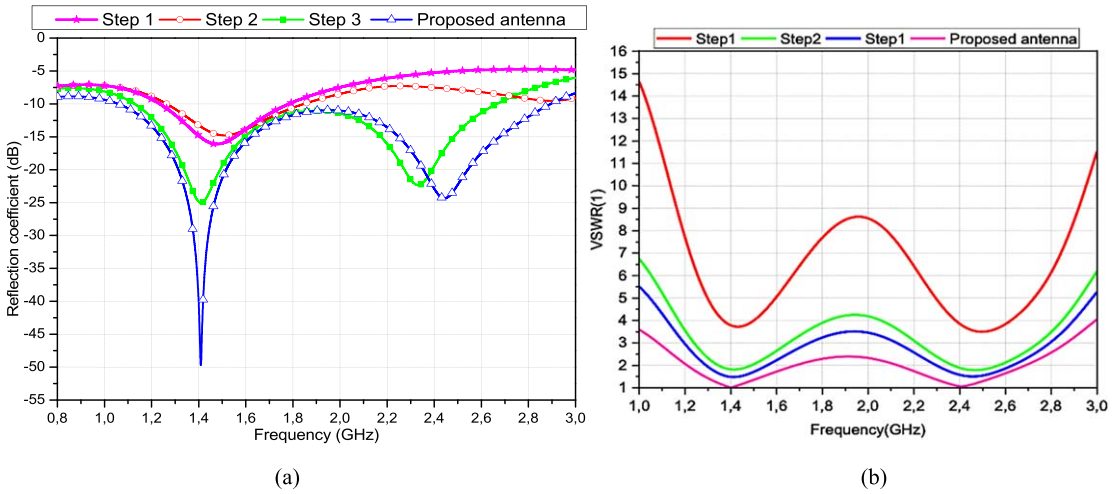

Figure 5. (a) Reflection coefficient and (b) VSWR for each designing step.

The power reflected by the antenna is quantified using the Voltage Standing Wave Ratio (VSWR), which directly depends on the reflection coefficient S11S11. For optimal antenna performance, the VSWR should ideally remain within the range of 1 to 2 [2]. Throughout the optimization process, a comprehensive VSWR analysis was conducted at each iteration, along with the evaluation of S11S11. The relationship between VSWR and the reflection coefficient is given by the following equation:

$$\mathrm{VSWR} = \frac{1 + |S_{11}|}{1 - |S_{11}|} \tag{1}$$

Figure 5(b) presents the frequency in GHz on the x-axis and the VSWR on the y-axis. To ensure optimal antenna performance, the VSWR value is 1.02 at 2.4 GHz and 1 at the resonance frequency of 1.4 GHz. This behavior confirms that as the VSWR approaches 1, reflection losses are minimized, which corresponds to a low S11 value, indicating a strong impedance match. The results demonstrate that the optimized antenna achieves VSWR values close to 1, confirming the effectiveness of the design at the targeted resonance frequencies.

2.4. Equivalent circuit model

To analyze the wideband behavior of the ultra-wideband antenna, an equivalent circuit model was created using the Advanced Design System (ADS), as illustrated in figure 6(a). This model is based on the Degraded Foster Canonical (DFC) framework [3], which is a well-established method for characterizing ultra-wideband

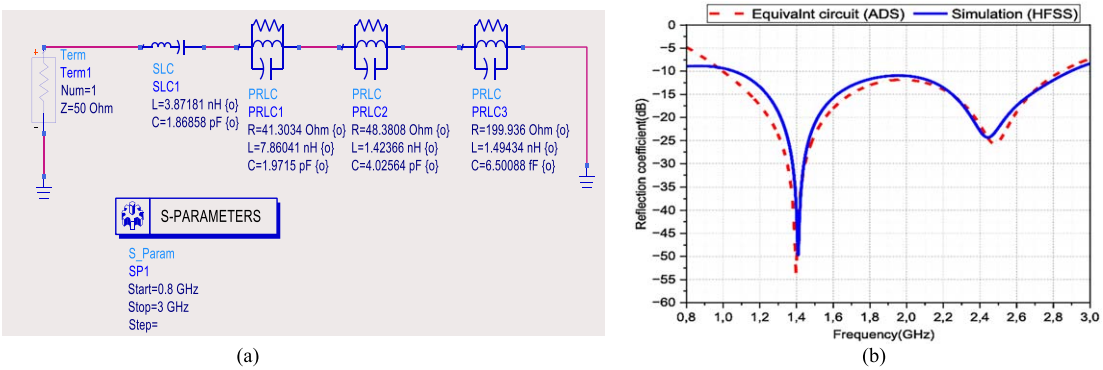

Figure 6. (a) Equivalent circuit representation of the proposed antenna using lumped elements. (b) Comparison of the reflection coefficient between HFSS simulations and the circuit model in ADS.

antennas. A wideband antenna is modeled as a radiating structure with multiple closely spaced resonances, where adjacent frequency bands may partially overlap. Each resonance is represented by parallel-connected RLC lumped elements. To achieve a wideband response, multiple parallel RLC circuits are cascaded, each corresponding to a specific resonance band. In figure 6(a), the capacitance and inductance define the fundamental resonance of the antenna, while the remaining higher-order resonances are captured by three additional parallel RLC circuits connected in series. The resistances model the radiation losses at their respective resonance frequencies. These losses are related to the energy radiated by the antenna during its operation at specific frequencies. The first R1L1C1 circuit ensures the impedance matching across the operating band, the second R2C2L2 regulates the lower-frequency response of the antenna, and the third R3C3L3 controls the behavior at higher frequencies. The component values of the equivalent circuit are detailed in the table presented in figure 6(b). The component values, provided in figure 6(b), were verified by comparing the model's response with full-wave electromagnetic simulations carried out in HFSS after optimization in ADS.

2.5. Simulation and measurement implantation scenarios

The ultra-miniaturized implantable antenna design, both with and without an integrated system, was developed using HFSS and CST simulators. The process of simulation and measurement is shown in figure 7. Initially, the antenna was positioned inside a synthetic homogeneous muscle phantom with dimensions of 100 mm × 60 mm × 100 mm, as seen in figure 7(a). Table 1 [34] details the electromagnetic properties for various tissues such as the stomach, heart, and intestines. The antenna's performance was evaluated using a 3656D Vector Network Analyzer, which operates within the 300 kHz to 20 GHz range, as depicted in figure 7(c). To further validate the antenna's performance in a realistic biological environment, the antenna was integrated into commercially sourced minced pork obtained from a supplier near Casablanca, Morocco. The minced pork was used to mimic the dielectric properties of human tissue due to its similar water and fat content, which closely resemble the properties of muscle tissue at microwave frequencies. The S11 response during the integration of the antenna into the minced pork is shown in figure 7(d). The results demonstrated a stable impedance match and consistent performance across the operating frequency bands. To assess how the electronic components affect antenna performance, a device model was created in HFSS, including the case, antenna, electronic assembly, sensors, batteries, and power management unit, as depicted in figure 7(a). The simulated results aligned closely with the measured results, confirming the accuracy of the design and its suitability for implantation in biomedical applications.

This study evaluated the antenna's effectiveness by measuring S11 values in different human body tissues. The results demonstrate that the designed antenna exhibits excellent adaptation characteristics in all four types of tissues. A slight impedance mismatch was observed in the small intestine due to its high conductivity, but the antenna effectively maintains resonance and covers the designated frequency bands. Moreover, the antenna consistently delivers robust performance, even with manageable frequency adjustments caused by the high-water content and increased permittivity of the stomach. The antenna remains effective for all these organs, maintaining optimal performance across diverse anatomical environments.

2.6. Parametric analysis

This section is dedicated to the parametric evaluation of the proposed wideband implantable antenna. Parametric analysis of an antenna serves as a method to optimize and customize the dimensional parameters in response to various scenarios. During this parametric analysis, we maintain the use of the same uniform

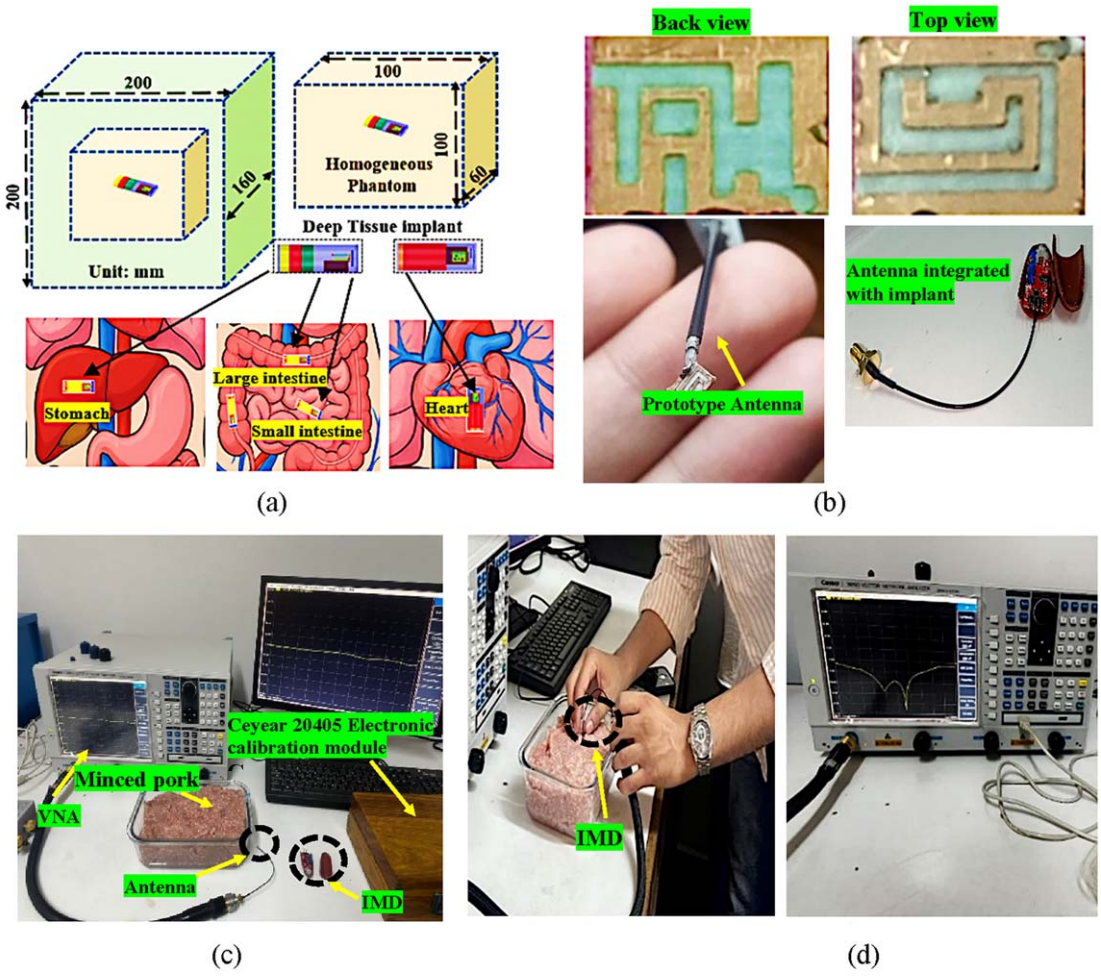

Figure 7. Simulations and measurements of implantation environments: (a) Antenna implantation within a homogeneous phantom with dimensions of 100 mm × 100 mm × 60 mm (b) Prototypes of the proposed antenna and 3D-printed capsule housing dummy electronics. (c) Measurement setup for the reflection coefficient of the antenna without the system in free space. (d) Measurement setup for the reflection coefficient of the antenna with the CP system positioned in minced pork.

Table 1. Electromagnetic properties of human body tissues.

Parameters	Permittivity 1.4 GHz 2.4 GHz	Conductivity 1.4 GHz 2.4 GHz
Small intestine	57.1 54.4	2.44 3.17
Large intestine	56.1 53.9	1.34 2.09
Stomach	63.9 62.2	1.44 2.21
Heart	57.5 54.8	1.51 2.26

equivalent phantom, characterized by consistent dielectric properties and dimensions for each medium, as previously detailed and depicted in figure 7(a). Furthermore, the antenna is positioned within the phantom to monitor how variations in antenna design parameters affect the reflection coefficient and impedance matching. Regarding our proposed antenna, the crucial parameters considered in this parametric analysis include the feeding point's location, the length of the patch side strips (L_{1-2}), and the dimensions of the ground slots ($C_{1\text{-}2\text{-}3}$), as outlined in figures 2(a) and (b). While a comprehensive examination of each parameter is beyond the scope of this article, it is essential to emphasize that, based on the specified parameters, our observations affirm the judicious selection of all parameters. Moreover, the proposed antenna is shown to be highly adaptable according to these parameters, as we will discuss further.

2.6.1. Impacts of the position of the feed

The impact of altering the position of the antenna's feeding point on S_{11} and impedance matching is graphically represented in figures 8(a) and (b) respectively. It becomes evident that the antenna's impedance matching

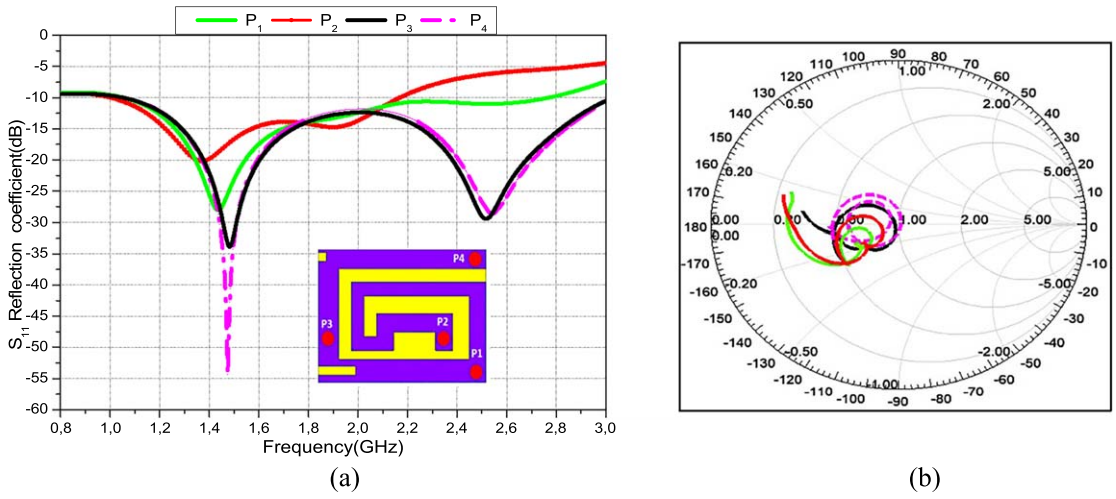

Figure 8. Influence of variations in feeding point position on (a) S11 and (b) impedance matching.

across the extensive operating bandwidth is substantially affected by the feeding point's placement. The impeccable impedance matching achieved by the proposed antenna experiences disruption as the feeding point transitions from the right corner to the left corner. For a more comprehensive grasp of this phenomenon, the impedances associated with these various feeding point positions are graphed on the Smith chart, as seen in figure 8(b). At position 1, the antenna exhibits a capacitive impedance, which requires an upward shift of the impedance trajectory loop to reduce the capacitance. When the position was changed from 2 to 3, a slight transition from capacitive to inductive impedance behavior was observed in the impedance loop. Notably, at position 4, the size of the impedance loop increased, indicating a substantial and stable impedance match over a wide frequency range. From a frequency band perspective, it is evident that the influence of the feeding point is essential to create a multi-resonant antenna. The antenna resonates at a single frequency of approximately 1.41 GHz when in position 1. A second resonance, but with relatively high S_{11} values, appears around 1.9 GHz when the antenna is in position 2. The antenna behaves as a dual-band antenna in position 3, with improved impedance matching. Finally, when the antenna is positioned at position 4, its adaptability is greatly enhanced, and its operating frequencies coincide with the intended ones.

2.6.2. Variations in the side strips length (L1-2) of patch

In order to attain optimal performance within the specified operating frequencies, precise adjustments were made to the dimensions of the slots on the plate, specifically L1 and L2. The variation in the S11 response of the wideband antenna as a function of L1 and L2 is illustrated in figure 9(a). It becomes evident that when the L1-L2 pair is held constant at L1 = 0.6 mm and L2 = 0.2 mm, the antenna showcases a broad bandwidth with favorable impedance matching, in alignment with its resonant frequencies. However, it's worth noting that impedance matching displays limited sensitivity to changes in the values of L1 and L2, as depicted in the Smith chart in figure 9(b). Furthermore, for the configuration where L1 = 0.6 mm and L2 = 0.2 mm, the size of the impedance loop expands. This signifies a substantial and stable impedance match across the entire frequency spectrum, indicating enhanced performance and consistent impedance characteristics.

2.6.3. Variations in the side strips length (C1-2-3) of ground

The investigation of the ground plane slot (C1-2-3) on the behavior of the proposed antenna has revealed significant insights, as showcased in figure 10. By varying the lengths of the ground plane slot (C1-2-3), we can readily adjust both resonant frequencies, as evidenced by the S11 curve. Notably, as C123 increases, there is a noticeable leftward shift in the resonance frequencies. Conversely, reducing C123 leads to a narrower spacing between neighboring bands, resulting in improved coupling. However, it is important to note that this narrower spacing also causes degraded reflection coefficients. Despite the changes in ground plane slot lengths, the antenna's impedance matching remains relatively less sensitive to variations in C_{123}, as clearly depicted in figures 10(b), (d),(f) of the Smith chart. This characteristic ensures robust performance over a range of configurations and contributes to the antenna's adaptability in real-world scenarios. Moreover, we observe the remarkable alignment of both resonance frequencies when C1, C2, and C3 are set to 0.8 mm, 0.8 mm, and 1 mm, respectively. This specific configuration has been deliberately selected due to its desirable characteristics, demonstrating optimal resonance frequencies and favorable coupling properties. The ability to fine-tune the

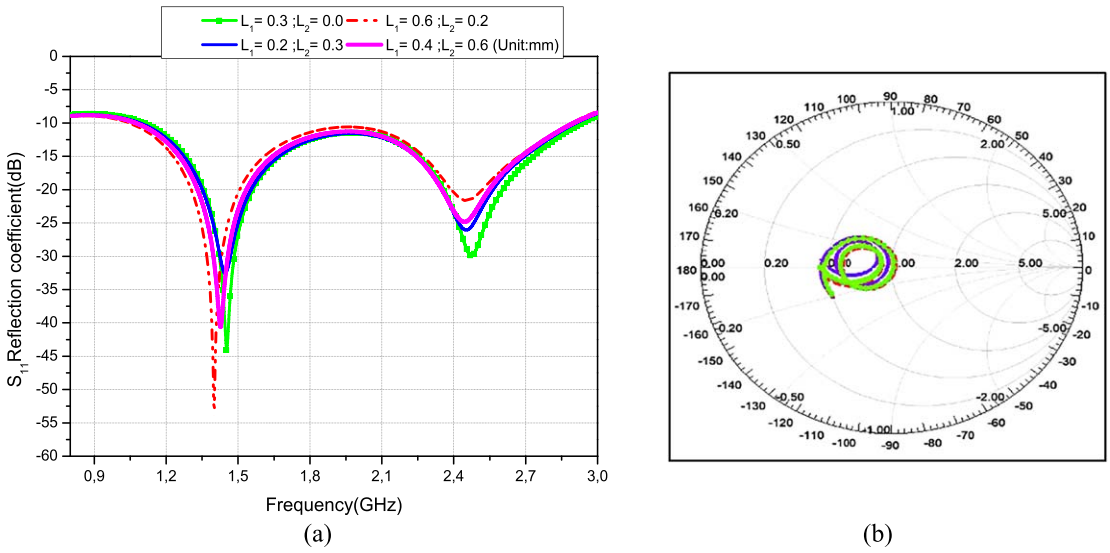

Figure 9. Influence of variations in L1-2 on S11 (a) and in impedance matching (b).

antenna's behavior through the manipulation of ground plane slot lengths enhances its versatility and suitability for various medical telemetry applications. These findings underscore the importance of carefully considering the ground plane slot design in optimizing the performance of implantable biomedical antennas.

3. Results and discussion

Implantable antennas often face significant frequency detuning when integrated with implantable medical devices (IMDs). Addressing this challenge, wideband (UWB) antennas have been proposed to mitigate frequency detuning, as discussed in [15]. The main objective of this study was to design an exceptionally compact antenna capable of maintaining stable impedance matching over a wide bandwidth, specifically optimized for effective operation within the human body. The antenna's optimization was initially carried out in a homogeneous phantom using High-Frequency Structure Simulator (HFSS) version 2023.R2. Subsequently, its performance was evaluated through simulations in a homogeneous phantom using CST Microwave Studio. Experimental validation was conducted by fabricating a prototype antenna, and the results closely matched the simulation outcomes. The antenna underwent careful testing in various anatomical regions, including the stomach, small and large intestines, heart, and other segments of the gastrointestinal system, as depicted in figure 7. Figure 11 presents a comparative analysis of the reflection coefficients exhibited by the antenna in these different environments. It is evident that the antenna consistently maintains stable impedance matching over a wide frequency range in all simulated scenarios. The observed bandwidths for the small intestine, large intestine, stomach, heart, and pork meat were 1567 MHz, 1591 MHz, 1557 MHz, 1836.8 MHz, and 1520 MHz, respectively. These results affirm the viability of the proposed wideband antenna for inclusion in implantable medical devices (IMDs). Additionally, figure 12 provides a visual representation of the radiation patterns of the wideband antenna as modeled in various scenarios. Despite variations in implantation sites, the gain polar patterns exhibit a similar omnidirectional character, with variations primarily in maximum values. Notably, at the operating frequency of 2.45 GHz, the radiation patterns maintain an omnidirectional nature in both the horizontal (H) and elevation (E) planes. However, antenna performance is significantly impacted when situated within the human body, primarily due to a notable reduction in efficiency. As reported in [35], the principal causes of this degradation include the absorption of electromagnetic radiation and substantial interaction between the antennas and surrounding tissues. The extent of this impact varies in intensity depending on the specific tissue type and depth of implantation. Consequently, the radiation efficiency of implanted antennas often drops well below -20 dB (1%) [36], representing a substantial decline from their performance in free-space conditions.

The simulation results demonstrate a significant variation in peak gain across different anatomical environments at 2.4 GHz. The observed peak gain for the heart was −19.92 dBi, which is relatively high compared to other locations. This higher gain can be attributed to the composition and structure of cardiac tissues, which appear to attenuate the electromagnetic signal less. In contrast, the peak gains observed in the large intestine, small intestine, and stomach were −21 dBi, −24 dBi, and −24 dBi, respectively. These lower values

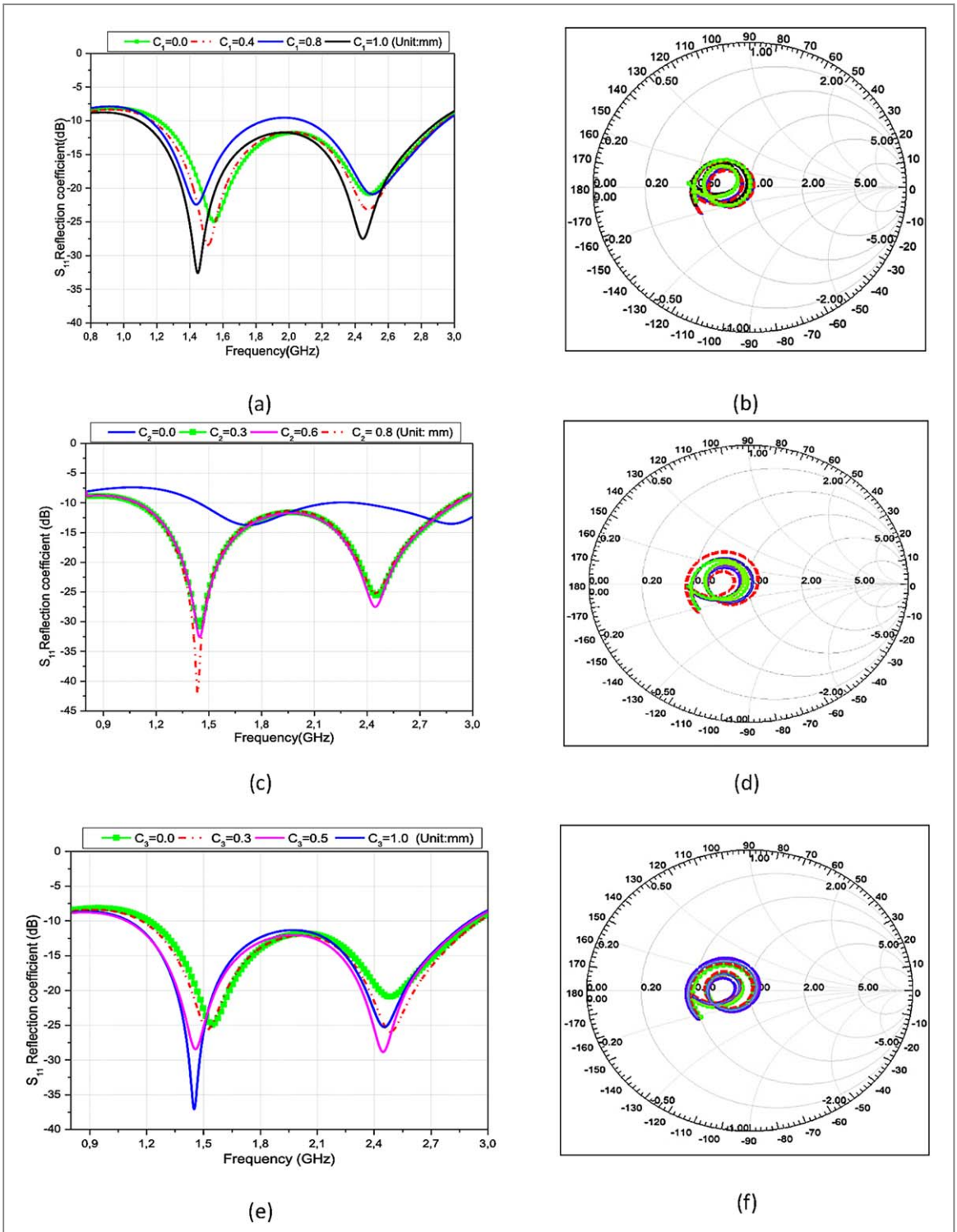

Figure 10. Influence of variations in C1 on (a) S11 and (b) impedance matching. Influence of variations in C2 on (c) S11 and (d) impedance matching. Influence of variations in C3 on (e) S11 and (f) impedance matching.

indicate greater signal attenuation, likely due to higher electromagnetic absorption and increased interaction between the antenna and surrounding tissues in these regions. These results underscore the importance of the implantation site in optimizing the communication performance of implantable medical devices. The variability in peak gain across different implantation sites must be carefully considered during the design and placement of such antennas to ensure reliable and efficient communication.

Figure 13 provides a visual representation of the radiation efficiency of the proposed implantable antenna under study. Remarkably, in both scenarios, the radiation efficiency surpasses −40 dB across the entire bandwidth. This indicates that, despite the challenges posed by the implantation, the antenna is still able to maintain a relatively efficient radiation performance. Such observations are critical in understanding the

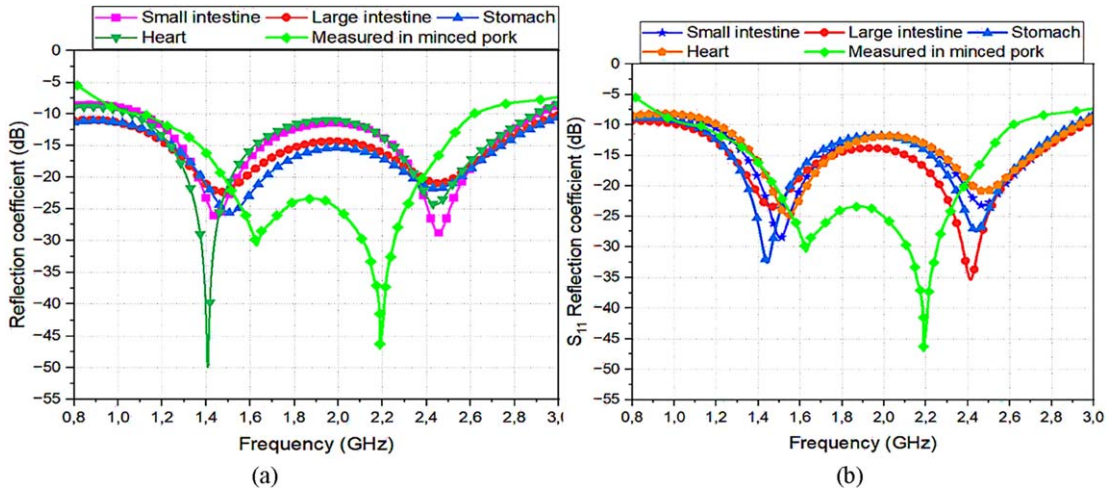

Figure 11. Comparison of reflection coefficient S11 under HFSS (a) and (b) CST.

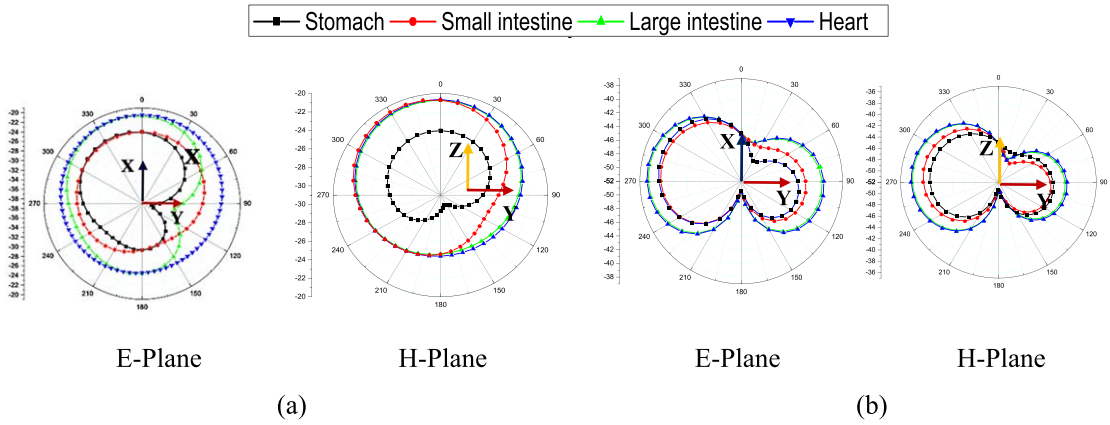

Figure 12. 2D polar radiation patterns. (a) 2.45 GHz. (b) 1.4 GHz.

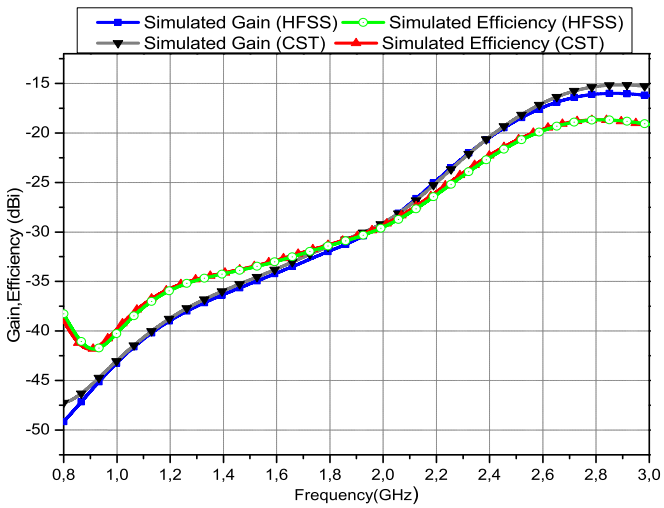

Figure 13. Gain and radiation efficiency of the proposed antenna under HFSS and CST.

antenna's behavior in the human body and guiding the optimization of its design for enhanced performance. It is worth noting that achieving and maintaining acceptable radiation efficiency levels are essential in implantable antennas to ensure reliable and effective wireless communication within the body. By studying the radiation

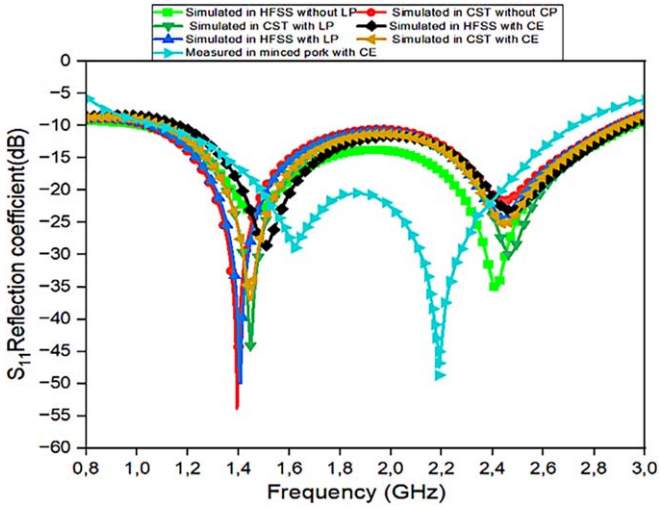

Figure 14. Coupling effects due to metallic components of the system on the wideband antenna performance.

efficiency characteristics under different conditions and tissue types, valuable insights can be gained to make informed design choices and further enhance the overall performance and reliability of implantable antenna systems.

3.1. Coupling analysis

The close proximity of the device components to the recommended wideband antenna necessitates an investigation into coupling phenomena between these components and the antenna. It is imperative to comprehend the impact and sensitivity of our antenna to such interactions. Within the scope of this coupling analysis, simulations are employed to explore potential implications and sensitivity of our antenna to the presence of neighboring device components. We delve into how the proximity of these device components to the antenna may give rise to interference, signal degradation, or alterations in the antenna's characteristics. Through a comprehensive examination of coupling issues, we can make informed design decisions and optimize the layout of device components to minimize any undesirable interactions with the wideband antenna. The ultimate objective is to ensure peak antenna performance while mitigating any adverse effects on its functionality. This coupling analysis will contribute to enhancing the overall performance and reliability of the proposed system by facilitating seamless integration between the device components and the antenna. As indicated in figure 14, it is evident that the proposed antenna remains relatively unaffected by the coupling effects, even under the worst-case scenario where the antenna directly contacts the implant components.

3.2. SAR analysis and tissue effects

A crucial facet of adhering to the biomedical device safety directives outlined by the IEEE pertains to the assessment of Specific Absorption Rate (SAR). The IEEE has established strict thresholds of 1.6 W kg^{-1} and 2 W kg^{-1} for 1 g and 10 g tissue masses, respectively, with the primary aim of safeguarding patient well-being [37, 38]. Accordingly, our investigation encompassed SAR computations within a phantom model featuring the stomach, small intestine, large intestine, heart, and resonance frequencies, as depicted in figure 15. A power transmission of 1 W was employed to generate the SAR data. It is imperative to note that, in order to align with the specified guidelines, the maximum input power for 1 g tissues should not exceed 10 mW (equivalent to 10 dBm) at 1.4 GHz and 8.1 mW (equivalent to 9.1 dBm) at 2.45 GHz. This ensures that SAR values remain within the established safety margins. While the calculated input power values do not precisely match the recommended figures, it is critical to underscore that implantable antennas are subject to stringent input power limitations of 25 μW, as articulated in [14, 24]. These computations unequivocally demonstrate that the SAR values associated with the implanted antenna conform to the IEEE guidelines and are deemed suitable for utilization in Body-Mounted Implant (BMI) devices. Table 2 provides a comprehensive overview of the estimated SAR values and the upper allowable input power levels for the specified implant locations within the 2.45 GHz and 1.4 GHz. The human body plays a critical role in the operation of implantable medical devices (IMDs), acting as a highly lossy medium.

Table 1 illustrates how the electrical characteristics of its tissues change based on the operation frequency. As mentioned in [39], human body tissues have high permittivity and conductivity, which greatly contributes to attenuation losses within the body.

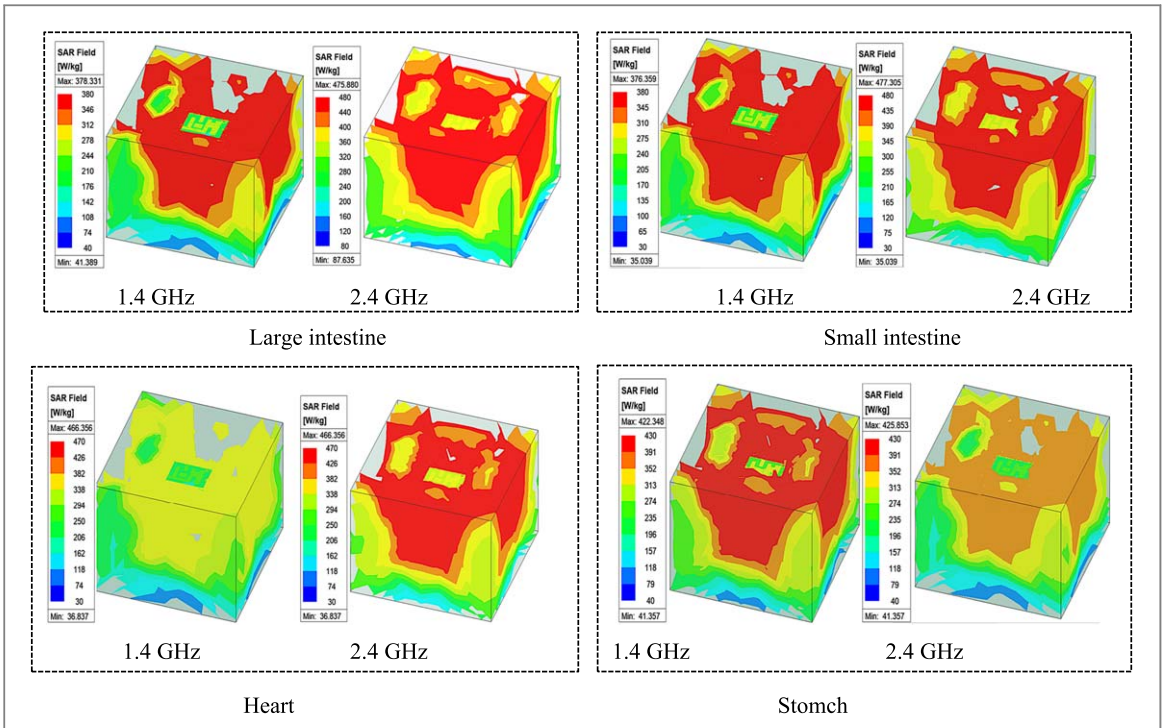

Figure 15. 3D analysis of specific absorption rates in the heart, stomach, small and large intestines of a human model.

Table 2. Maximum SAR (1-g) values (for 1 w input power) and allowable maximum input powers.

Body tissue	Peak SAR (W/Kg) 1.4 GHz 2.4GHz	Maximum allowable power (mW) 1.4 GHz 2.4GHz
Small intestine	376.36 477.3	1.5 1.7
Large intestine	373.33 475.88	1.45 1.67
Heart	466.35 466.35	1.38 1.63
Stomach	422.35 425.85	1.41 1.6

3.3. Link budget analysis for biotelemetry

The assessment of telemetry range between the implantable device and an external base station holds paramount significance in ensuring the dependable transmission of biological data. Nonetheless, the computation of the link budget involves accounting for multiple loss factors, notably encompassing free-space losses, cable losses, as well as losses attributed to antenna materials and mismatches [5]. A diagrammatic representation of the arrangement for link budget calculation is depicted in figure 16.

A link margin exceeding 20 dB is imperative for ensuring reliable communication. The calculation of link margins involves employing the Friis equation to determine the disparity between the antenna power (AP) and the requisite antenna power (RP). One method for computing RP is outlined as follows:

$$R_p = B_r + \frac{E_b}{N_0} + KT \tag{2}$$

In this context, the variables Eb/No, K, To, and Br represent phase shift keying, temperature, bit rate, Boltzmann's constant, and Br, respectively. Conversely, the determination of Ap can be expressed as follows:

$$A_p(dB) = P_{TX} + G_{TX} + G_{RX} - L_f - P_L \tag{3}$$

The parameters P_{TX}, G_{TX}, and G_{RX} represent, respectively, the transmitter power fixed at 4 dBm, the transmitter antenna gain, and the implantable receiver antenna gain. The losses due to free space and polarization mismatch are denoted by L_f and P_L, respectively. The free space loss, L_f, is typically dependent on the separation distance (d) between the transmitting and receiving antennas. The following equations can be used to calculate these losses:

The parameters P_{TX}, G_{TX}, and G_{RX} correspond to the transmitter power (4 dBm), the gain of the transmitting antenna, and the gain of the implantable receiving antenna, respectively. The losses L_f and P_L account for free-space attenuation and polarization mismatch, respectively. The following equations are used to

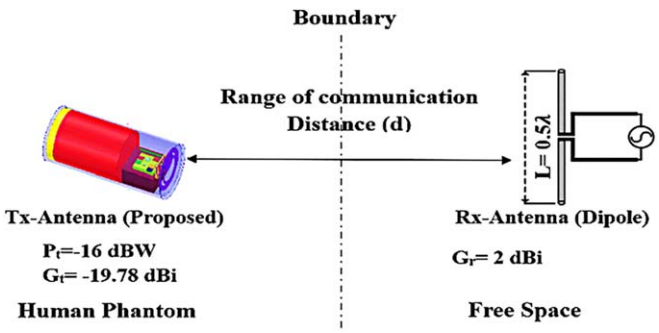

Figure 16. Conceptual diagram for the link budget analysis.

Table 3. The key parameters taken into consideration for conducting a link budget analysis.

Parameters	Variables	Values
Resonance frequency	f_0(GHz)	1.4–2.4
Noise Power Density	N_0(dB/Hz)	−203.93
Transmitter Power	P_{TX}(dB_m)	−16
Polarization mismatch loss	$P_L(dB)$	1
Temperature	T_0(Kelvin)	273
Path Loss	L_f(dB)	Distance dependent
Transmitter antenna Gain	G_{TX}(dB_i)	$G_{TX}(1.4\ GHz)$=−36 dBi $G_{TX}(2.4\ GHz)$ = −19.78 dBi
Receiver antenna Gain	G_{RX}(dB_i)	G_{RX} = 2 dBi
Boltzmann Constant	K	1.38×10^{-23}
Available Power	$A_P(dB)$	Distance dependent
Bit rate	B_r	78 bits
Required Power	$R_P(dB)$	Adaptive (Bit rate)
Antenna Power	$A_P(dB)$	Adaptive (Distance)
Margin	$A_P - R_P(dB)$	figure 17
Path loss exponent	δ	*1.5*
Shadowing effect	$S(dB)$	*0*

compute these losses:

$$L_f(dB) = 10\delta \times \log\left(\frac{d}{d_0}\right) + 10 \times \log\left(\frac{4\pi d_0}{\lambda_0}\right)^2 + S_{(dB)} \quad (4)$$

The link margin formula considers key parameters: d is the distance between antennas, δ is the path loss exponent based on the environment, λ_0 represents the free-space wavelength, and d_0 is defined as $d_0 = \frac{2L^2}{\lambda_0}$, where L denotes the maximum antenna dimension in the radiation direction. Random dispersion is accounted for by S. The study utilizes an ideal half-wave dipole antenna with a 2 dBi gain as the receiver, simplifying the analysis by neglecting polarization and impedance mismatch losses. Table 3 presents the connection budget, while figure 17 demonstrates the link budget calculation. To ensure reliable data transmission, the link margin must exceed 0 dB, with a 20 dB margin considered for error-free communication. A conservative transmission power of 25 μW is selected to minimize interference with other devices operating at the same frequency.

A closer examination of the connection margin graph reveals that as data rates increase, so does the achievable communication range. Consequently, the proposed system exhibits the capability to effectively establish communication over a distance of 20 meters, even at high data rates of 78 Mbps. Antenna systems designed for high data rates, such as this one, find practical applications in domains like surgery, capsule endoscopy, and other scenarios where a substantial transmission throughput is imperative. Figure 18 shows that the received signal strength for both frequencies is plotted as a function of distance, demonstrating the ability of the proposed antenna to communicate effectively with the transmitting antenna. The results presented in the same figure highlight an intriguing trend: when the proposed antenna operates at 1.4 GHz, it has a greater range than when it operates at 2.4 GHz. This distinction stems from a fundamental characteristic of radio waves, namely their wavelength. At 1.4 GHz, radio waves have a longer wavelength, giving the proposed antenna a greater ability to penetrate obstacles and maintain stable communication over long distances. Conversely, at

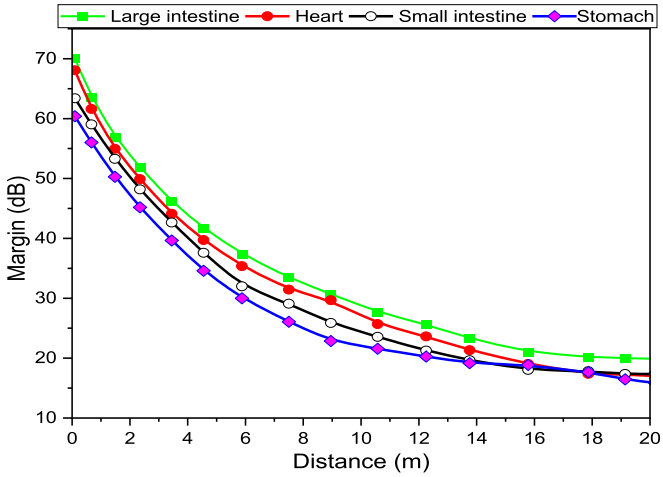

Figure 17. Link budget analysis of the antenna in homogeneous phantoms.

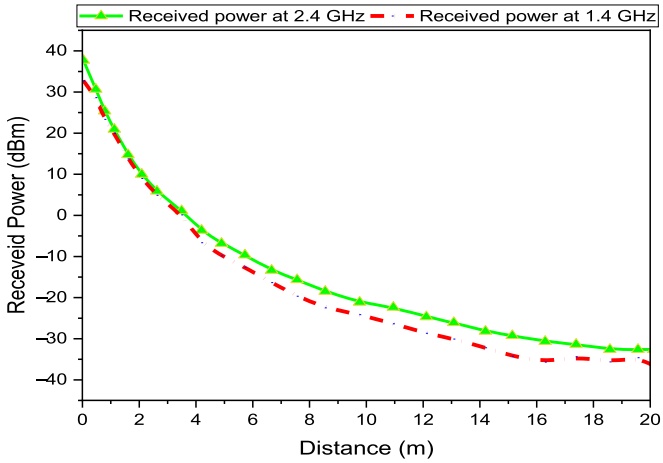

Figure 18. Received signal strength against distance.

2.4 GHz, range decreases due to the increased absorption of waves by obstacles and their greater sensitivity to interference.

These results underline the crucial importance of frequency selection in the design of biomedical antennas for wireless communication applications. This nuanced understanding of the interaction between frequency and range offers substantial perspectives for the optimal design of biomedical antennas in various application contexts.

Table 4 compares the performance of the proposed antenna with recent studies, emphasizing compliance with implant specifications, particularly size constraints critical for implantable devices. The proposed antenna meets these stringent requirements and ranks among the smallest designs reported. Operating in dual-band mode, it leverages two frequency bands for distinct signaling types, enhancing the system's flexibility and functionality. This study enables the evaluation of the coupling rate between the antenna and the implant, a critical factor that can disrupt the signal and affect the overall system performance. By accurately quantifying this coupling, it becomes possible to minimize its impact through parametric optimization and the encapsulation of the antenna in biomedical materials, thereby enhancing the implant's electromagnetic compatibility. Without this analysis, the results would remain somewhat detached from reality, as the antenna is inherently linked to the implant. An inaccurate estimation of the coupling effect could compromise the efficiency of the device, highlighting the necessity of this study to ensure optimal performance under real implantation conditions. Encased in a biocompatible material, the antenna ensures safe integration into the human body, addressing a limitation in many existing designs. Moreover, it complies with Specific Absorption Rate (SAR) safety standards, ensuring patient protection. Despite these strict constraints, the antenna achieves exceptional performance,

Table 4. Proposed antenna comparison with recent works.

References	Volume (mm^3)	Freq.(GHz)	Bandwidth (MHz)	Gain (dBi)	SAR (W/kg) 10 g-Avg 1 g-Avg	Device study
[40]	$7 \times 7 \times 0.2$	2.45	1038.7	−20.71	−289.76	No
[41]	$3 \times 3 \times 0.5$	2.45	528	−24.9	32.3 10.8	Yes
[42]	$2.2 \times 2.15 \times 0.78$	2.45	384,48	−27.76	−1.55	Yes
		5.8	553,9	−16.40	−1.58	
[43]	$4 \times 3.3 \times 0.5$	1.2	1646.8	−34.44	84.0 691.1 87.35 798.21	Yes
		2.45		−19.78		
[44]	$21 \times 13.5 \times 0.254$	2.45	47.7	−15.8	−0.78	No
[45]	$3.3 \times 4 \times 0.38$	2.45	288	−22.5	−783	No
This Work	$\mathbf{3 \times 4 \times 0.5}$	**1.4**	**1836.8**	**−36**	**79.8 376.36**	**Yes**
		2.45		**−19.92**	**82.3 477.3**	

aligning with its design objectives to provide a compact, high-performance, and safe solution for implantable applications.

4. Conclusion

This paper introduces a compact wideband implantable antenna designed to operate at 2.45 GHz and 1.4 GHz, aimed at overcoming impedance mismatch challenges associated with variations in human tissue properties, age-related factors, and the specific needs of implantable medical devices (IMDs). By integrating open-ended slots in the antenna's patch and ground plane, the design achieves improved frequency tuning, impedance matching, and size reduction. To assess the antenna's practical performance, wave propagation studies were conducted in tissue models, followed by implantation in different human organ models for further validation. Compliance with IEEE C95.1-1999 safety standards was ensured through an analysis of Specific Absorption Rates (SAR) at the implant sites. Link margins were calculated to evaluate the communication range between the external base station and the antenna system. The antenna's design was verified through simulations using HFSS and CST tools, with experimental validation performed on prototypes within minced pork. The measured results closely aligned with the simulations, confirming the antenna's effectiveness and practicality for real-world implantable applications.

Acknowledgments

The authors would like to express their gratitude to the universities of Ibn Tofail and Cadi Ayyad in Morocco for their valuable support and collaboration. The authors also wish to thank Universiti Teknikal Malaysia Melaka (UTeM) and the Ministry of Higher Education (MOHE) of Malaysia for supporting this project.

Data availability statement

All data that support the findings of this study are included within the article (and any supplementary files).

ORCID iDs

Abdelmouttalib Bousrout https://orcid.org/0009-0000-0111-928X
Ahmed Jamal Abdullah Al-Gburi https://orcid.org/0000-0002-5305-3937

References

[1] Jasim M, Al-Gburi A J A, Hanif M, Dayo Z A, Ismail M M and Zakaria Z 2025 An extensive review on implantable antennas for biomedical applications: health considerations, geometries, fabrication techniques, and challenges *Alexandria Engineering Journal* **112** 110–39
[2] Ahmad S *et al* 2023 Novel implantable antenna with miniaturized footprint size for wideband biomedical telemetry applications *Freq.* **77** 293–301
[3] Zaki A Z A, Hamad E K I, Abouelnaga T G, Elsadek H A, Khaleel S A, Al-Gburi A J A and Zakaria Z 2023 Design and modeling of ultra-compact wideband implantable antenna for wireless ISM band *Bioengineering* **10** 216
[4] Soliman M M, Chowdhury M E H, Khandakar A, Islam M T, Qiblawey Y, Musharavati F and Nezhad Z E 2021 Review on medical implantable antenna technology and imminent research challenges *Sensors* **21** 3163

[5] Shah S A A and Yoo H 2018 Scalp-implantable antenna systems for intracranial pressure monitoring *IEEE Trans. Antennas Propag.* **66** 2170–3
[6] Ahmad S, Manzoor B, Paracha K N, Haider S, Liaqat M, Al-Gburi A J A, Ghaffar A, Alibakhshikenari M and Dalarsson M 2022 A wideband bear-shaped compact size implantable antenna for in-body communications *Appl. Sci.* **12** 2859
[7] Liu C, Guo Y-X and Xiao S 2012 Compact dual-band antenna for implantable devices *IEEE Antennas Wireless Propag. Lett.* **11** 1508–11
[8] Rahman A *et al* 2016 Electromagnetic performances analysis of an ultra-wideband and flexible material antenna in microwave breast imaging: to implement a wearable medical bra *Sci. Rep.* **6** 38906
[9] Kiourti A and Nikita K S 2014 Antennas and RF communication *Handbook of Biomedical Telemetry* (Wiley) 209–51
[10] Kiourti A, Psathas K A and Nikita K S 2014 Implantable and ingestible medical devices with wireless telemetry functionalities: a review of current status and challenges *Bio Electro Magn.* **35** 1–15
[11] Kim J and Rahmat-Samii Y 2004 Implanted antennas inside a human body: Simulations, designs, and characterizations *IEEE Trans. Microw. Theory Techn.* **52** 1934–43
[12] Srinivasan S S *et al* 2023 A vibrating ingestible bioelectronic stimulator modulates gastric stretch receptors for illusory satiety *Sci. Adv.* **9** eadj3003
[13] Soontornpipit P, Furse C M and Chung Y C 2004 Design of implantable microstrip antenna for communication with medical implants *IEEE Trans. Microw. Theory Techn.* **52** 1944–51
[14] Faisal F, Zada M, Ejaz A, Amin Y, Ullah S and Yoo H 2019 A miniaturized dual-band implantable antenna system for medical applications *IEEE Trans. Antennas Propag.* **68** 1161–5
[15] Fan Y, Huang J, Chang T and Liu X 2018 A miniaturized four-element MIMO antenna with EBG for implantable medical devices *IEEE J. Electromagn. RF. Microw. Med. Biol.* **2** 226–33
[16] Bashir Z, Zahid M, Abbas N, Yousaf M, Shoaib S, Asghar M A and Amin Y 2019 A miniaturized wide band implantable antenna for biomedical application *Proc. UK/China Emerg. Technol. (UCET)* 14
[17] Faisal F and Yoo H 2019 A miniaturized novel-shape dual-band antenna for implantable applications *IEEE Trans. Antennas Propag.* **67** 1161–5
[18] Al-Gburi A J A *et al* 2024 Superconductive and flexible antenna based on a tri-nanocomposite of graphene nanoplatelets, silver, and copper for wearable electronic devices *J. Sci. Adv. Mater Devices.* **9** 100773
[19] Abdullah Al-Gburi A J, Ismail M M, Naba Jasim M, Buragohain A and Alhassoon K 2024 Electrical conductivity and morphological observation of hybrid filler: silver-graphene oxide nanocomposites for wearable antenna *Opt. Mater.* **148** 114882
[20] Al-Gburi A J A *et al* 1992 SAR flexible antenna advancements: highly conductive polymer-graphene oxide-silver nanocomposites *Prog. Electromagn. Res. M* **127** 23–30
[21] Saha P, Mitra D and Parui S K 2018 A circularly polarized implantable monopole antenna for biomedical applications *Prog. Electromagn. Res. C* **85** 167–75
[22] Bao Z, Guo Y-X and Mittra R 2017 Single-layer dual-/tri-band inverted antennas for conformal capsule type of applications *IEEE Trans. Antennas Propag.* **65** 7257–65
[23] Zada M and Yoo H 2018 A miniaturized triple-band implantable antenna system for biotelemetry applications *IEEE Trans. Antennas Propag.* **66** 7378–82
[24] Shah I A, Zada M and Yoo H 2019 Design and analysis of a compact-sized multiband spiral-shaped implantable antenna for scalp implantable and leadless pacemaker systems *IEEE Trans. Antennas Propag.* **67** 4230–4
[25] Ding S, Koulouridis S and Pichon L 2020 Implantable wireless transmission rectenna system for biomedical wireless applications *IEEE Access* **8** 195551–8
[26] Iqbal A, Al-Hasan M, Mabrouk I B, Basir A, Nedil M and Yoo H 2021 Biotelemetry and wireless powering of biomedical implants using a rectifier integrated self-diplexing implantable antenna *IEEE Trans. Microw. Theory Tech.* **69** 3438–51
[27] Das S and Mitra D 2018 A Compact wideband flexible implantable slot antenna design with enhanced gain *IEEE Trans. Antennas Propag.* **66** 4309–14
[28] Durgun A C, Balanis C A, Birtcher C R and Allee D R 2011 Design, simulation, fabrication and testing of flexible bow-tie antennas *IEEE Trans. Antennas Propag.* **59** 4425–35
[29] Kim S and Shin H 2019 An ultra-wideband conformal meandered loop antenna for wireless capsule endoscopy *J. Electromagn. Eng. Sci.* **19** 101–6
[30] Lin H Y, Takahashi M, Saito K and Ito K 2013 Performance of implantable folded dipole antenna for in-body wireless communication *IEEE Trans. Antennas Propag.* **61** 1363–70
[31] Huang F-J, Lee C-M, Chang C-L, Chen L-K, Yo T-C and Luo C-H 2011 Rectenna application of miniaturized implantable antenna design for triple-band biotelemetry communication *IEEE Trans. Antennas Propag.* **59** 2646–53
[32] Bao Z, Guo Y-X and Xiao S 2020 Circular implantable antenna for biomedical applications *IEEE Antennas Wireless Propag. Lett.* **19** 119–23
[33] Liu C, Guo Y-X and Xiao S 2012 Minuscule dual-band antenna for implantable devices *IEEE Antennas Wireless Propag. Lett.* **11** 1508–11
[34] Hasgall P A, Di Gennaro F, Baumgartner C, Neufeld E, Lloyd B, Gosselin M C, Payne D, Klingenböck A and Kuster N 2022 Database for thermal and electromagnetic parameters of biological tissues *Version* **4** 1
[35] Soliman M M, Chowdhury M E, Khandakar A, Islam M T, Qiblawey Y, Musharavati F and Nezhad E Z 2021 Review on medical implantable antenna technology and imminent research challenges *Sensors* **21** 3163
[36] Nikolayev D, Zhadobov M and Sauleau R 2018 Impact of tissue electromagnetic properties on radiation performance of in-body antennas *IEEE Antennas Wireless Propag. Lett.* **17** 1440–4
[37] Chien T-F, Cheng C-M, Yang H-C, Jiang J-W and Luo C-H 2010 Development of nonsuperstrate implantable low-profile CPW-fed ceramic antennas *IEEE Antennas Wireless Propag. Lett.* **9** 599–602
[38] Ciuti G, Menciassi A and Dario P 2011 Capsule endoscopy: from current achievements to open challenges *IEEE Rev. Biomed. Eng.* **4** 59–72
[39] Kiourti A and Nikita K S 2017 A review of in-body biotelemetry devices: implantable, ingestible, and injectables *IEEE Trans. Biomed. Eng.* **64** 1422–30
[40] Abbas N, Shah S A A, Basir A, Bashir Z, Akram A and Yoo H 2022 Miniaturized antenna for high data rate implantable brain-machine interfaces *IEEE Access* **10** 66018–27
[41] Feng Y, Li Z, Qi L, Shen W and Li G 2022 A compact and miniaturized implantable antenna for ISM band in wireless cardiac pacemaker system *Sci. Rep.* **12** 238

[42] Bousrout A, Khabba A, Ibnyaich S, Mazri T, Habibi M and Sutikno T 2024 Ultra-miniaturized dual-band implantable antenna for retinal prosthesis *Indonesian Journal of Electrical Engineering and Computer Science (IJEECS* **36** v36.i2 760–76
[43] Bousrout A, Khabba A, Ibnyaich S, Mazri T, Habibi M and Sutikno T 2024 Compact miniaturized antenna design and development for a leadless cardiac pacemaker *TELKOMNIKA Telecommunication, Computing, Electronics and Control* **22** v22i6.25958
[44] Butt A D, Khan J, Ahmad S, Ghaffar A, Abdullah Al-Gburi A and Hussein M 2023 Single-fed broadband CPW-fed circularly polarized implantable antenna for sensing medical applications *PLoS One* **18** e0280042
[45] Bousrout A, Khabba A, El-Haryqy N, Ibnyaich S, Mazri T and Habibi M 2024 Compact miniaturized antenna design for enhanced data rates in implantable brain-machine interfaces *2024 Int. Conf. on Global Aeronautical Engineering and Satellite Technology (GAST)* 1–6